Journal of Translational Medicine

RESEARCH

Open Access

Chronic intermittent hypoxia impairs BM-MSC osteogenesis and long bone growth through regulating histone lactylation

Fang Chen[1†], Meizhen Gu[1†], Hongming Xu[1], Shasha Zhou[2], Zilu Shen[1], Xiaoyan Li[1*], Liangchao Dong[3*] and Pin Li[2*]

Abstract

Background Chronic intermittent hypoxia (CIH) caused by OSA often results in serious complications. However, the adverse effects of CIH on bone growth and development are often overlooked.

Methods CIH intervention was conducted using an OxyCycler model A84 system for 8 h per day (from 8:00 a.m. to 4:00 p.m.) over a period of 4 weeks. Body and femur lengths were measured, and micro-CT, histological analysis, and ELISA were performed to evaluate femoral development. Metabolomic, single-cell transcriptomic, Western blot, and ChIP–qPCR analyses were conducted to explore the potential mechanisms underlying CIH-induced inhibition of long bone growth. T0070907 was administered intraperitoneally (0.5 mg/kg) every two days to investigate its effect on long bone growth under CIH conditions.

Results Here, we showed that CIH stimulation during long bone development significantly inhibited long bone growth. Multiomics analysis revealed that CIH induces anaerobic glycolysis in bone marrow mesenchymal stem cells (BM-MSCs), promotes adipogenic differentiation, and reduces their osteogenic differentiation capacity. Mechanistic studies demonstrated that CIH-induced lactate accumulation enhances lactylation at histone H3 lysine 18 (H3K18) on the PPARγ promoter in BM-MSCs, leading to the transcriptional activation of PPARγ and a consequent imbalance between the adipogenic and osteogenic differentiation of BM-MSCs. The PPARγ inhibitor T0070907 could partially rescue long bone developmental disorders induced by CIH.

Conclusions Our findings reveal an epigenetic mechanism underlying CIH-induced long bone dysplasia and highlight T0070907 as a promising targeted therapeutic agent.

Keywords Chronic intermittent hypoxia, Bone development, BM-MSCs, Histone lactylation, PPARγ

[†]Fang Chen and Meizhen Gu contributed equally to this work.

*Correspondence:
Xiaoyan Li
lxyshchildren@163.com
Liangchao Dong
alextung3399@163.com
Pin Li
lipin2019@126.com

[1]Department of Otolaryngology-Head and Neck Surgery, Shanghai Children's Hospital, School of Medicine, Shanghai Jiao Tong University, Shanghai 200062, China
[2]Department of Endocrinology, Shanghai Children's Hospital, School of Medicine, Shanghai Jiao Tong University, Shanghai 200062, China
[3]Department of Orthopedics, Shanghai Children's Hospital, School of Medicine, Shanghai Jiao Tong University, Shanghai 200062, China

Background

Obstructive sleep apnea syndrome (OSAS) is a common chronic sleep-related respiratory disorder characterized by partial or complete obstruction of the upper airway during sleep, leading to chronic intermittent hypoxia (CIH) [1]. The incidence of OSAS in children is approximately 2–4%, with a peak onset age of 2–5 years [2]. CIH is an important pathological factor leading to a series of serious complications of OSAS, such as cardiovascular issues, metabolic disorders, and cognitive dysfunction [3–5]. Compared with these complications, the harm caused by CIH to bone growth and development is often overlooked. In children, during the critical period of growth and bone mass accumulation, the potential effects of CIH, such as delayed bone growth and reduced bone density, can cause irreversible damage [6]. Despite these concerns, the impact of OSAS on skeletal development remains underresearched.

Bone development is a highly coordinated process that is finely regulated by both systemic and local factors, in which bone marrow mesenchymal stem cells (BM-MSCs) play crucial roles [7]. BM-MSCs possess multilineage differentiation potential and can differentiate into both osteoblasts and adipocytes [8]. Under physiological conditions, BM-MSCs maintain the balance between osteogenic and adipogenic differentiation activities. However, under chronic hypoxic conditions, this balance is disrupted, leading to weakened osteogenic differentiation and ultimately affecting bone development [9]. However, the mechanism by which CIH impairs the osteogenic differentiation of BM-MSCs remains largely unknown.

The fate of BM-MSCs is strictly controlled by epigenetic mechanisms, such as histone methylation, acetylation and phosphorylation [10]. Studies have shown that alpha-ketoglutarate decreases the accumulation of H3K9me3 and H3K27me3, thereby increasing bone morphogenetic protein (BMP) signaling, promoting the osteogenic potential of BM-MSCs, and ameliorating osteoporosis [11]. Mechanical stimulation can regulate histone acetylation levels through HDAC1, promoting the osteogenic differentiation of BM-MSCs [12]. In recent years, a novel histone modification, histone lactylation, has gained increasing attention for its roles in various diseases, including cancer [13], tissue fibrosis [14], and neurodegenerative diseases [15]. However, the effects of histone lactylation on BM-MSC differentiation and its potential molecular mechanisms remain poorly understood. Exploring the potential roles of histone lactylation in bone growth and development may reveal novel therapeutic strategies for the treatment of bone dysplasia.

In the present study, we found that CIH significantly inhibited the development of long bones in mice, as evidenced by reduced femur length, decreased trabecular bone density, and lower levels of one turnover markers. Furthermore, we revealed that CIH induced a shift in the metabolic pattern of BM-MSCs toward anaerobic glycolysis while producing more lactate. The increased lactate upregulated the H3K18la level in the PPARγ promoter region in BM-MSCs, activating PPARγ gene transcription and thereby disrupting the balance of BM-MSC differentiation. The inhibition of PPARγ through targeted agents has been shown to rescue bone growth and mitigate bone loss caused by CIH.

Methods

Chronic intermittent hypoxia model

Eight-week-old female C57BL/6 mice were purchased from Shanghai Slac Laboratory Animal (Slac, Shanghai, China), housed in individual cages with a 12-h light/dark cycle and provided with standard food and water ad libitum. All procedures were approved by the Animal Ethics Committee of Shanghai Sixth People's Hospital.

The CIH intervention was conducted in identical chambers (OxyCycler model A84; BioSpherix, Parish, NY, USA) for 8 h per day (from 8:00 a.m. to 4:00 p.m.) over a period of 4 weeks. Hypoxia was induced by exposure to 8–10% O_2 for 240 s, followed by exposure to 21% O_2 for 120 s, as described previously [16]. For T0070907 treatment, the mice were intraperitoneally injected with 100 μl of either T0070907 (0.5 mg/kg) or vehicle every two days. Each week, the body length of the mice was measured, blood was collected through eyeball enucleation, and the femurs were isolated to measure their length and then used for subsequent studies.

Micro-CT scanning

The femur tissues were fixed in 4% paraformaldehyde and analyzed by micro-CT (Skyscan 1176, Bruker, Germany) at a resolution of 15.6 μm. The region of interest (ROI) was defined as the distal end of the femur. The bone volume per tissue volume (BV/TV%), trabecular number (Tb.N), trabecular thickness (Tb.Th), trabecular separation (Tb.Sp) and structure model index (SMI) of each sample were obtained using CTAn v1.9 software (Skyscan US, San Jose, CA).

Histology and immunohistochemical staining

Femur samples were fixed with 4% paraformaldehyde, embedded in paraffin, and sectioned at a thickness of 5 μm. The sections were then stained with hematoxylin and eosin (H&E), ALP, and TRAP as previously

described [17]. Three random growth plate regions were selected from the H&E-stained sections to measure the lengths of the proliferative zone (PZ), hypertrophic zone (HZ), and resting zone (RZ). The PZ, HZ and RZ lengths were evaluated independently by 3 researchers who were blinded to the groups. The ALP expression level and the number of $TRAP^+$ cells/mm^2 were calculated with ImageJ software.

For immunohistochemical staining, the sections were incubated overnight at 4°C with antibodies against collagen type I (Col I, 1:500, Abcam, ab316222) and osteocalcin (OCN, 1:200, Abcam, ab309521). After incubation with the appropriate secondary antibodies, the sections were developed with 3',3-diaminobenzidine (Sigma–Aldrich) and counterstained with hematoxylin. Protein expression levels were quantified using ImageJ software.

Enzyme-linked immunosorbent assay (ELISA)

The expression levels of BGP/OCN, PINP, β-CTX, TRAP, and OPG in the serum were measured using ELISA kits (Meimian, China) according to the manufacturer's instructions. The absorbance values were recorded at 450 nm using a microplate reader (Tecan Group AG, Männedorf, Switzerland).

Immunofluorescence staining

The femur sections were incubated overnight at 4 °C with antibodies against Osterix (OSX 1:200, Abcam, ab209484). After washing, the sections were incubated with an Alexa Fluor® 555-conjugated secondary antibody for 1 h at room temperature in the dark. Fluorescence was determined using a Zeiss 710 laser-scanning microscope (Zeiss, Thornwood, NY, USA).

Single-cell transcriptome sequencing

The femurs of the mice were dissected, and the attached muscle tissues were removed. A 3-mm-long segment of the metaphyseal region from the growth plate was taken from the femoral tissue and crushed using a mortar and pestle. The crushed tissue was digested with collagenase type I (2 mg/mL) for 30 minutes, filtered through a 70 μm cell strainer, washed with ice-cold PBS, and resuspended in DMEM medium. Sequencing libraries were prepared using a SeekOne® Digital Droplet Single Cell 3' Library Prep Kit (SeekGene, Beijing, China) and sequenced on the Illumina NovaSeq 6000 platform.

LC–MS/MS and GC–MS analyses

The metabolomic data analysis was performed by Shanghai Luming Biological Technology Co., Ltd (Shanghai, China). For LC–MS/MS analysis, an ACQUITY UPLC I-Class plus (Waters Corporation, Milford, USA) fitted with a Q Exactive mass spectrometer equipped with a heated electrospray ionization (ESI) source (Thermo Fisher Scientific, Waltham, MA, USA) was used to analyze the metabolic profiles in both ESI-positive and ESI-negative ion modes. For GC–MS analysis, the derivatized samples were analyzed on an Agilent 7890B gas chromatography system coupled to an Agilent 5977 A MSD system (Agilent Technologies Inc., CA, USA). A two-tailed Student's *t* test was used to verify whether the metabolites with differences between groups were significant. Differentially abundant metabolites with VIP values greater than 1.0 and *p* values less than 0.05 were selected. Differentially abundant metabolites were further used for KEGG pathway enrichment analysis.

Primary BM-MSC isolation and identification

Primary BM-MSCs were isolated from adult C57BL/6 mice as previously described [18]. Briefly, femurs were isolated under sterile conditions and washed three times with PBS. The bone marrow cavity was exposed by removing both ends of the femur and tibia. Both ends of the femur were cut to expose the bone marrow. The marrow was flushed out using a syringe filled with DMEM/F12 culture medium into a collection tube and then passed through a 70-μm cell strainer to remove debris. The cells were cultured in Gibco™ DMEM/F12 supplemented with 10% fetal bovine serum (Gibco, USA) and antibiotics (penicillin 100 IU/mL and streptomycin 100 mg/mL) in 5% CO_2 at 37 °C. After 48 h, the culture medium was replaced to remove unattached cells. BM-MSCs at passage numbers 3–5 were used. BM-MSCs were identified using flow cytometry. BM-MSCs (passage 3) were incubated with anti-CD90 (Thy1) (BioLegend, UK), anti-CD29 (FITC) (BioLegend, UK), and anti-CD45 (APC) (BioLegend, UK) antibodies at 4 °C for 30 min. After washing, the cells were analyzed by flow cytometry (Beckman Coulter, USA).

Alizarin Red staining and Oil Red O staining

BM-MSCs were cultured under normoxic or hypoxic conditions (2% oxygen) while undergoing osteogenic or adipogenic induction, or the PPARγ inhibitor T0070907 or vehicle was added during osteogenic or adipogenic induction.

For Alizarin Red staining, BM-MSCs were subjected to 14 days of osteogenic induction, after which the cells were fixed for 30 min at room temperature. Following washing, the cells were stained using an Alizarin Red S staining kit (Beyotime, China) according to the manufacturer's instructions.

For Oil Red O staining, BM-MSCs were subjected to 14 days of adipogenic induction, after which the cells were fixed for 30 min at room temperature. Following

washing, the cells were stained using an Oil Red O staining kit (Beyotime, China) according to the manufacturer's instructions. Images were captured using a microscope (Nikon, Japan).

Lactate concentration assay

Decalcified bone tissue was homogenized using a TissueMaster™ Tissue Homogenizer (Beyotime, China). The homogenate was resuspended in prechilled PBS and then centrifuged at 4 °C and 2,000 rpm for 10 min. The supernatant obtained from the centrifugation, or the BM-MSC supernatant, was used to measure the lactate concentration in an automatic biochemical analyzer (ABL80 FLEX analyzer).

Quantitative real-time PCR (qPCR)

In brief, total RNA was extracted using TRIzol reagent (Invitrogen, USA), and its concentration was measured using a NanoDrop spectrophotometer (Thermo Fisher, USA). Quantitative PCR amplification was then performed on an ABI PRISM QuantStudio 7 Flex (Thermo Fisher, USA) using SYBR Premix (Takara, Japan). The primers used were as follows:

Bglap, (forward) 5'-CACTCCTCGCCCTATTGGC-3'; Bglap, (reverse) 5'-CCCTCCTGCTTGGACACAAAG-3'; Col1a1, (forward) 5'-GCTCCTCTTAGGGGCCACT-3'; Col1a1, (reverse) 5'-ATTGGGGACCCTTAGGCCAT-3'; Adipoq, (forward) 5'-TGTTCCTCTTAATCCTGCCCA-3'; Adipoq, (reverse) 5'-CCAACCTGCACAAGTTCCCTT-3'; Plin1, (forward) 5'-CTGTGTGCAATGCCTATGAGA-3'; Plin1, (reverse) 5'-CTGGAGGGTATTGAAGAGCCG-3'; GAPDH, (forward) 5'-AGGTCGGTGTGAACGGATTTG-3'; GAPDH, (reverse) 5'-TGTAGACCATGTAGTTGAGGTCA-3'.

Histone extraction

Histones were extracted using a Histone Extraction Kit (Abcam, UK) according to the manufacturer's instructions. Briefly, the cells were harvested and pelleted by centrifugation at 1,000 rpm for 5 min at 4 °C. The cell pellet was resuspended in 3 volumes of lysis buffer and incubated on ice for 30 min. The mixture was subsequently centrifuged at 12,000 rpm for 5 min at 4 °C, after which the supernatant fraction was transferred to a new vial. A 0.3 volume of the Balance-DTT Buffer was added to the supernatant immediately. The samples were quantified by measuring the absorbance at 230 nm.

Western blot

The cells were lysed using RIPA lysis buffer (Beyotime, China) supplemented with protease inhibitor (Roche, Mannheim, Germany). The protein concentration was determined by BCA assay (Beyotime, China). The primary antibodies used included the following: RUNX2 (Abcam, ab236639), PPARγ (Abcam, ab272718), H3K9la (PTM Bio, PTM-1419RM), H3K14la (PTM Bio, PTM-1414RM), H3K18la (PTM Bio, PTM-1427RM), H3K23la (PTM Bio, PTM-1413RM), H3K27la (PTM Bio, PTM-1428), GAPDH (Cell Signaling Technology, #8884), and Histone H3 (Cell Signaling Technology, #9715). Densitometric quantification was carried out using ImageJ software.

Chromatin immunoprecipitation (ChIP)

A ChIP assay was performed using a ChIP Kit (Millipore, catalog #17-10085) following the manufacturer's protocol. In brief, the cells were fixed and resuspended in 0.5 mL of lysis buffer containing a protease inhibitor cocktail and then subjected to sonication. The number of DNA fragments in the solubilized chromatin preparation ranged from 400 to 800 bp. Immunoprecipitation was performed overnight using anti-H3K18la (PTM Bio, PTM-1427RM) or normal rabbit IgG as a negative control. The antigen–antibody complexes were pulled down using protein A/G agarose beads. The DNA–protein crosslinking reactions were reversed by incubation with 5 M NaCl at 65 °C for 6 h, and the DNA from each sample was then purified and subjected to PCR.

Statistical analysis

Statistical analysis was performed using SPSS 20.0 software. An independent-samples t test was used for comparisons between two groups. One-way analysis of variance (ANOVA) followed by a post hoc Tukey test was used to compare multiple groups. All values are presented as the mean ± SD. Differences between groups were considered significant at $P < 0.05$.

Results

CIH inhibits the development of long bones in mice

To investigate the effects of CIH on long bone development in mice, a CIH model was established in 4-week-old mice. The results revealed that CIH led to significant decreases in body weight and body length compared with those of control mice (Fig. 1A-C), and femur length was noticeably shorter after four weeks of CIH (Fig. 1D).

In addition, micro-CT revealed that the CIH group presented a reduction in trabecular bone quantity and disordered arrangement in the metaphyseal trabecular bone region of the distal femur (Fig. 1E). BV/TV, Tb.N, and Tb.Th were significantly lower in the CIH group than in the control group, whereas Tb.Sp and SMI were somewhat greater (Fig. 1F). These findings suggest that CIH leads to a decrease in trabecular bone density in the long bones of mice. Histological analysis

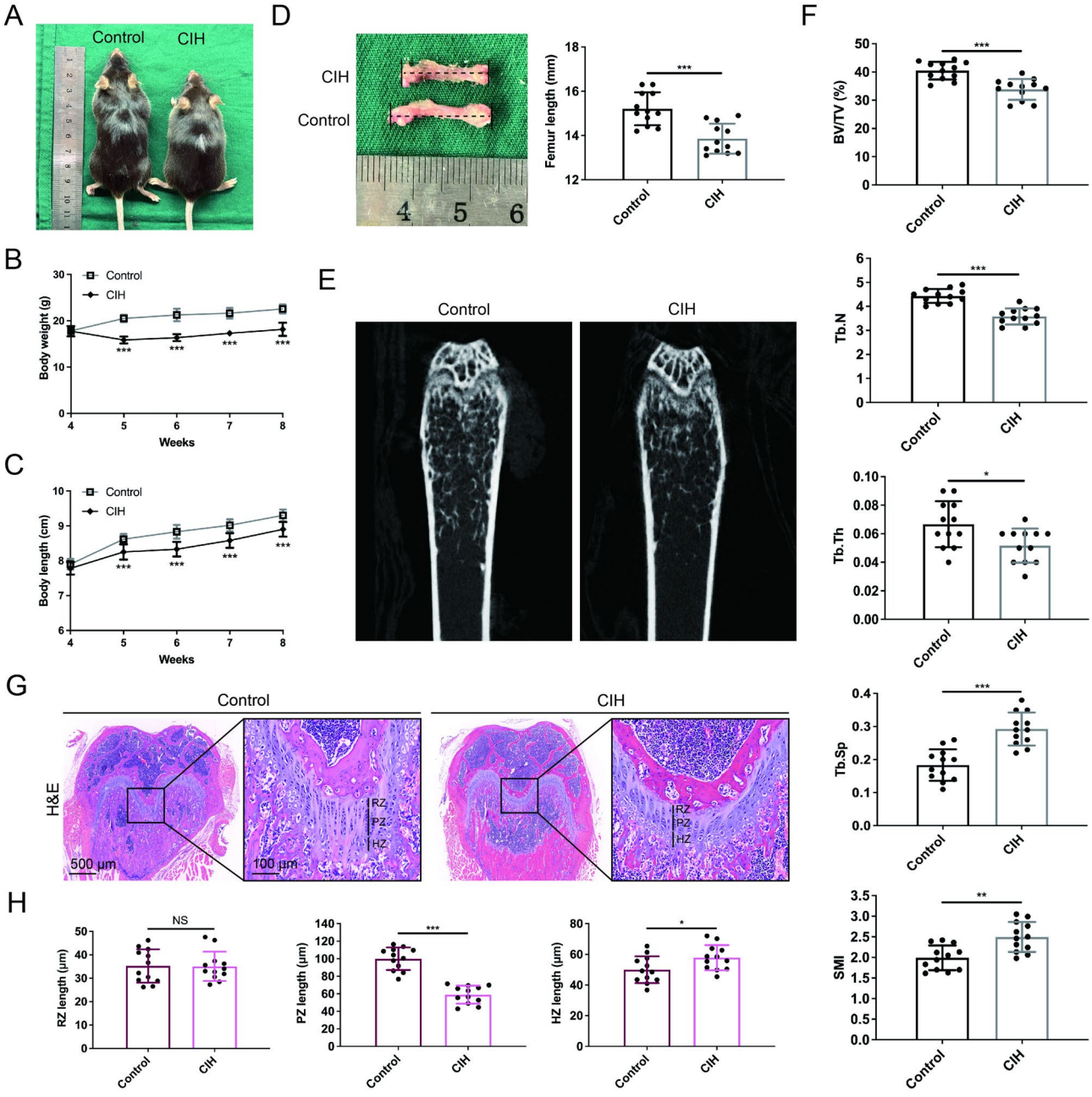

Fig. 1 CIH impairs long bone growth in mice. (**A**) Macroscopic images of mice after 4 weeks of CIH or control treatment. (**B**, **C**) The quantification of body weight and body length at all examined time points. (**D**) Macroscopic images of the mouse femur and quantification of femur length. (**E**) Micro-CT images of the mouse femur after 4 weeks of CIH or control treatment. (**F**) The quantification of bone volume per tissue volume (BV/TV%), trabecular number (Tb.N), trabecular thickness (Tb.Th), trabecular separation (Tb.Sp) and structure model index (SMI). (**G**) H&E-stained images of the distal femur after four weeks of CIH or control treatment. (scale bar = 500 μm). Zoomed-in images show the growth plate cartilage region. (zoom scale bar = 100 μm). (**H**) The quantification of the lengths of the resting zone (RZ), proliferative zone (PZ), and hypertrophic zone (HZ). Data are presented as mean ± SD ($n = 12$ biologically independent animals). *$P < 0.05$; **$P < 0.01$; ***$P < 0.001$

revealed that the proliferative zone (PZ) of the growth plate cartilage in the CIH group was significantly shorter than that in the control group, with a reduction in flattened proliferative chondrocytes (Fig. 1G, H). Moreover, the hypertrophic zone (HZ) was slightly increased in length, with an increased number of columnar hypertrophic chondrocytes (Fig. 1G, H). These findings suggest that CIH reduces endochondral ossification at the metaphysis of the femur in growing mice.

CIH downregulates the expression of osteogenesis-related proteins

Given the ability of CIH to inhibit long bone development, we examined the expression of osteogenesis-related proteins in the growth plate region of the distal femur. The expression of ALP in the CIH group was significantly lower than that in the control group (Fig. 2A). Additionally, the number of TRAP-positive cells was also reduced following CIH (Fig. 2B). These data suggest that CIH primarily inhibits osteoblast-mediated bone formation while also exerting a moderate inhibitory effect on bone resorption. The immunohistochemistry results showed that, compared with those in control mice, the expression levels of Col

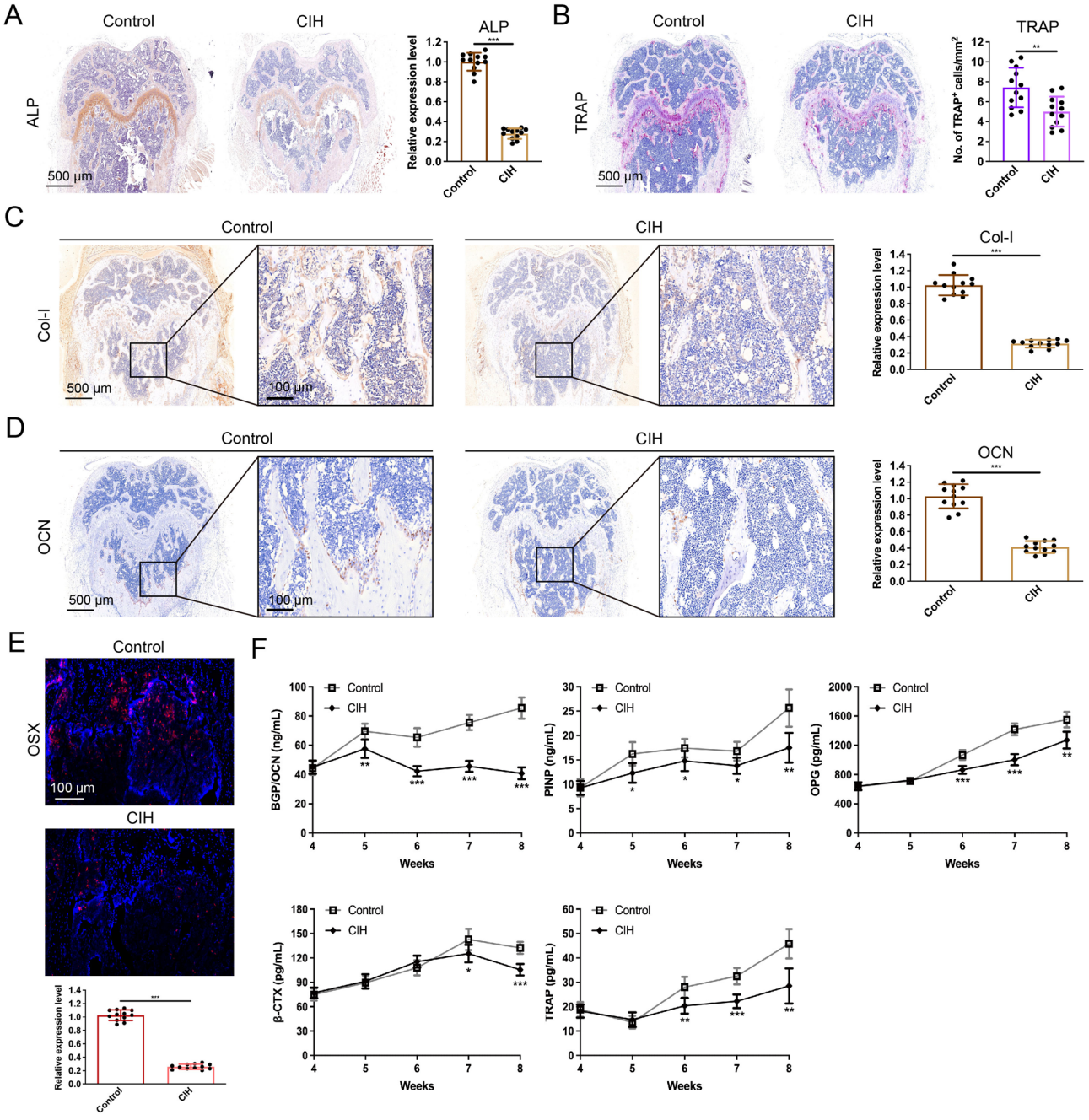

Fig. 2 CIH downregulates the expression of bone turnover markers. (**A**, **B**) ALP- and TRAP-stained images of the distal femur after four weeks of CIH or control treatment, along with expression quantification. (scale bar = 500 μm). (**C**, **D**) Images and quantitative analysis of immunohistochemical staining of collagen COL I and OCN in the CIH and the control group. (scale bar = 500 μm, zoom scale bar = 100 μm). (**E**) Images and quantitative analysis of immunofluorescence staining for OSX in the CIH and the control group. OSX is labeled in red. (Scale bar = 100 μm). (**F**) Serum bone turnover marker levels at all examined time points. Data are presented as mean ± SD ($n = 12$ biologically independent animals). *$P < 0.05$; **$P < 0.01$; ***$P < 0.001$

I and OCN were significantly lower in the CIH group, indicating that CIH inhibits long bone osteogenesis (Fig. 2C, D). OSX is an osteoblast-specific transcription factor essential for bone formation. Therefore, we analyzed the expression of OSX in the distal femoral growth plate region using immunofluorescence. The results demonstrated that OSX expression was significantly lower in the CIH mice than in the control mice (Fig. 2E). Furthermore, we examined changes in the levels of serum bone turnover markers during CIH. We found that the levels of serum bone formation markers (BGP/OCN, PINP, and OPG) were significantly lower in the CIH group than in the control group and that the levels of bone resorption markers (β-CTX and TRAP) were also lower in the CIH group than in the control group after two weeks of CIH (Fig. 2F). These findings indicate that CIH inhibits bone turnover in growing mice, primarily affecting the bone formation process.

CIH increases glycolysis and adipogenic differentiation in BM-MSCs

To further explore the underlying mechanisms by which CIH attenuates bone growth, single-cell transcriptome analysis was performed (Fig. 3A). Our data revealed that cells in mouse femoral tissue can be

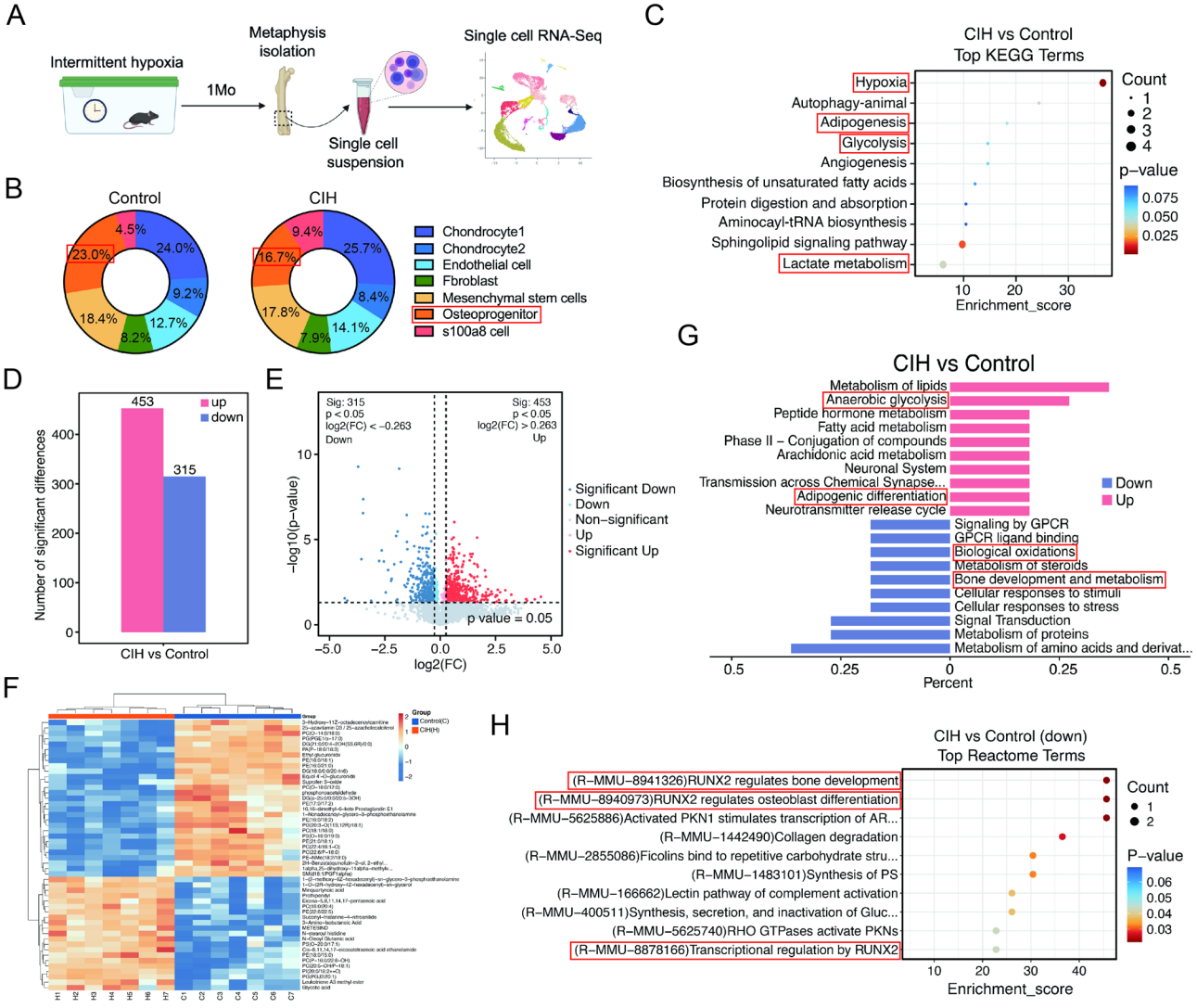

Fig. 3 CIH enhances glycolysis and adipogenic differentiation in BM-MSCs. (**A**) Schematic diagram of single-cell transcriptome sequencing of femoral tissue. (**B**) The proportions of each BM-MSC subpopulation between the CIH group and the control group. (**C**) KEGG assay results of significantly upregulated pathways of differentially expressed genes in BM-MSCs between the CIH group and the control group. (**D**) The number of metabolites with significant differences between the CIH group and the control group. (**E**, **F**) Volcano map and Heatmap of differential metabolites between the control group and the CIH group. (**G**) KEGG assay results showing the top 10 upregulated and downregulated pathways of differentially expressed genes in femoral tissues between the CIH group and the control group. (**H**) Reactome assay results of significantly downregulated pathways of differentially expressed genes in femoral tissues between the CIH group and the control group

categorized into 15 types. In addition to immune and hematopoietic cells, key cell types include BM-MSCs, endothelial progenitor cells (EPCs), and smooth muscle cells. Given the crucial role of BM-MSCs in osteogenesis, we conducted a more detailed analysis of these cells. We found that BM-MSCs can be classified into six subsets: chondrocytes, osteoprogenitors, fibroblasts, MSCs, endothelial cells, and S100a8 high-expressing cells. Although most subpopulations were not significantly different between the CIH and control groups, the proportion of osteoprogenitors in the CIH group was 16.7%, which was significantly lower than the 23.0% observed in the control group (Fig. 3B). These findings suggest that CIH may inhibit the differentiation of BM-MSCs into osteoprogenitor cells, thereby suppressing osteogenesis. Furthermore, KEGG analysis revealed significant activation of pathways related to hypoxia, adipogenesis, glycolysis, and lactate metabolism in BM-MSCs from the CIH group. (Fig. 3C). These findings indicate that CIH may affect glucose metabolism in BM-MSCs, potentially impacting osteogenesis.

To further investigate the potential impact of CIH on cell metabolism, we performed a metabolomic analysis of femoral tissue. Compared with those in the control group, 453 metabolites were upregulated and 315 metabolites were downregulated in the CIH group (Fig. 3D-F). We subsequently conducted KEGG analysis and selected the top 10 upregulated and downregulated pathways with the smallest *P* values for comparison. The results revealed a significant upregulation of anaerobic glycolysis and adipogenic differentiation pathways in the CIH group, whereas biological oxidation, bone development, and metabolism pathways were downregulated (Fig. 3G). Further reactome enrichment analysis showed that pathways such as "RUNX2 regulates bone development" and "RUNX2 regulates osteoblast differentiation" were significantly downregulated in the CIH group (Fig. 3H). These findings are consistent with the single-cell sequencing results, indicating that CIH induces a metabolic shift in femoral tissue toward anaerobic glycolysis, promoting adipogenesis while impairing osteogenesis.

CIH disrupts the balance between the osteogenic and adipogenic differentiation of BM-MSCs

Single-cell sequencing and metabolomic analysis suggested that CIH enhances the adipogenic differentiation of BM-MSCs while reducing their differentiation into osteoprogenitors. Therefore, we collected femoral tissue after four weeks of CIH induction and isolated BM-MSCs to evaluate the effects of CIH on BM-MSC differentiation (Fig. 4A, B). The results revealed that, compared with those in the control group, the intracellular lipid droplet content in the BM-MSCs in the CIH group markedly increased after adipogenic induction (Fig. 4C). In contrast, after osteogenic induction, alizarin red staining revealed markedly less calcium salt deposition in the CIH group than in the control group (Fig. 4D). qPCR revealed that BM-MSCs from the CIH group presented significantly lower expression levels of the osteogenesis-related genes *Bglap* and *Col1a1* than those from the control group did, whereas the expression levels of the adipogenesis-related genes *Adipoq* and *Plin1* were markedly increased (Fig. 4E). These findings suggest that following CIH induction, BM-MSCs exhibit significantly reduced osteogenic potential and enhanced adipogenic differentiation.

Furthermore, we examined the expression levels of key transcription factors involved in osteogenesis and adipogenesis, namely, RUNX2 and PPARγ. Western blot analysis revealed that CIH significantly reduced the expression of RUNX2 while increasing the expression of PPARγ in BM-MSCs (Fig. 4F). These results indicate that CIH may alter the differentiation potential of BM-MSCs by regulating the expression of key transcription factors involved in osteogenic/adipogenic differentiation.

CIH upregulates the H3K18la level of the PPARγ gene

Our metabolomics analysis revealed that CIH enhances glycolysis in BM-MSCs, with lactate as the main product. We measured the lactate level in femoral tissue following CIH. ELISA analysis revealed that the lactate content in the femoral tissue of the CIH group was significantly greater than that in the control group at all the assessed time points during CIH stimulation (Fig. 5A). Additionally, the lactate concentration in the cell supernatant of BM-MSCs from the CIH group was markedly greater than that in the control group (Fig. 5B). These results suggest that 4 weeks of CIH stimulation can alter the metabolic profile of BM-MSCs, leading to increased lactate production.

In recent years, emerging evidence has indicated that lactate is an important epigenetic regulator that induces histone lactylation [14]. Based on these findings, we hypothesized that CIH might influence the differentiation trajectory of BM-MSCs by regulating histone lactylation. Our Western blot analysis revealed that BM-MSCs from the CIH group had higher lactylation levels at multiple histone lactylation sites (H3K9la, H3K14la, H3K18la, H3K23la, H3K27la) than those from the control group did, with H3K18la showing the most significant increase (Fig. 5C). Moreover, we examined common histone methylation (H3K4me3, H3K9me3, and H3K27me3) and acetylation (H3K9ac and H3K27ac) sites in BM-MSCs from the CIH and

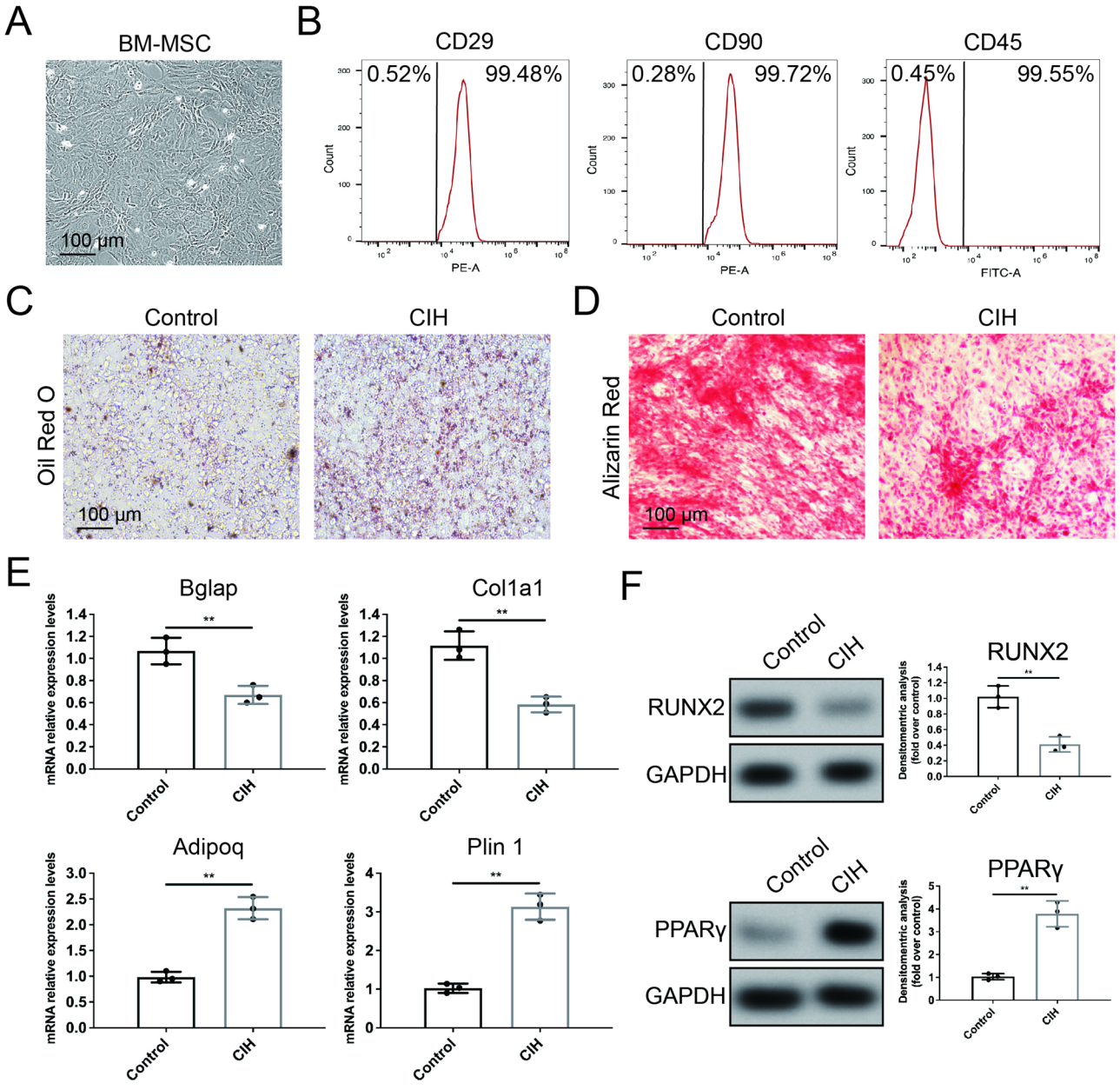

Fig. 4 CIH inhibits the osteogenic differentiation of BM-MSCs. (**A**) Images of phase-contrast microscopy of BM-MSCs. (**B**) Identification of surface antigen-specific markers of BM-MSCs. (**C**, **D**) Oil Red O and Alizarin Red staining images of BM-MSCs isolated from mice in the CIH or control group. (scale bar = 100 μm). (**E**) Relative RNA expression levels of osteogenic and adipogenic marker genes in BM-MSCs isolated from mice in the CIH or control group. (**F**) The protein levels of RUNX2 and PPARγ in BM-MSCs isolated from mice in the CIH or control group. Data are presented as mean ± SEM ($n = 3$ independent experiments). $^{**}P < 0.01$

control groups and found no significant differences between them (Fig. 5D). To further investigate whether hypoxia contributes to the increased H3K18la level, we subjected normal BM-MSCs to hypoxic treatment. As expected, after 72 h of hypoxia, the lactylation level of H3K18la was significantly increased (Fig. 5E). However, the addition of 2-DG during hypoxia suppressed the hypoxia-induced H3K18la upregulation (Fig. 5F). In addition, we examined the expression of the histone acetyltransferase p300, the "writer" of histone lactylation, and found that p300 expression was markedly higher in CIH-derived BM-MSCs than in control BM-MSCs (Fig. 5G). Similarly, compared with normoxic control BM-MSCs, hypoxia-treated BM-MSCs presented increased p300 levels (Fig. 5H). These results suggest that, in addition to lactate, p300 may also be involved in the CIH-induced increase in lactylation at the H3K18 site.

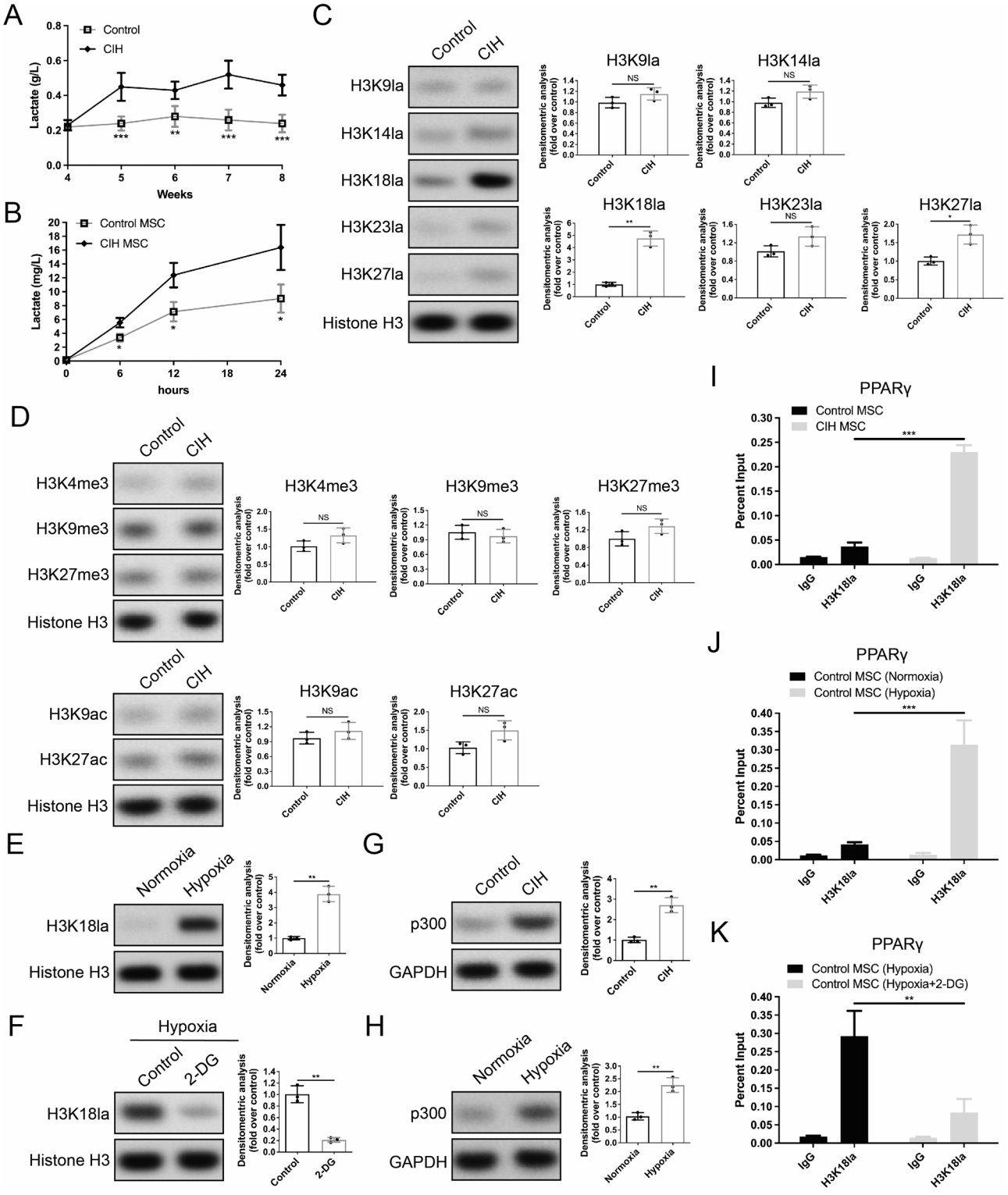

Fig. 5 (See legend on next page.)

Considering that CIH can upregulate PPARγ expression, we speculated that this might result from increased histone lactylation in the PPARγ promoter region. Our ChIP–qPCR results revealed that, compared with control BM-MSCs, BM-MSCs from the CIH group presented significantly higher H3K18la levels in the PPARγ promoter region (Fig. 5I). Furthermore, in normal BM-MSCs, hypoxia markedly

(See figure on previous page.)

Fig. 5 CIH increases the H3K18la level in the promoter region of the PPARγ gene in BM-MSCs. (**A**, **B**) Lactate levels in femoral tissue and the supernatant of BM-MSCs in the control and CIH groups. (**C**) The levels of H3K9la, H3K14la, H3K18la, H3K23la, and H3K27la in BM-MSCs isolated from mice in the CIH or control group. (**D**) The levels of H3K4me3, H3K9me3, H3K27me3, H3K9ac and H3K27ac in BM-MSCs isolated from mice in the CIH or control group. (**E**) The H3K18la levels in BM-MSCs isolated from control mice following normoxia or hypoxia treatment. (**F**) The H3K18la levels in BM-MSCs under hypoxic conditions with or without 2-DG treatment. (**G**) The protein levels of p300 in BM-MSCs isolated from mice in the CIH or control group. (**H**) The protein levels of p300 in BM-MSCs isolated from control mice following normoxia or hypoxia treatment. (**I**) ChIP assay confirming the increased H3K18la level in the PPARγ promoter region of BM-MSCs isolated from CIH mice. (**J**) ChIP assay confirming the increased H3K18la level in the PPARγ promoter region of BM-MSCs under hypoxic conditions. (**K**) ChIP assay confirming that 2-DG blocks the hypoxia-induced upregulation of H3K18la levels in the PPARγ promoter region. Data in (**A**) are presented as mean ± SD ($n = 12$ biologically independent animals). Data in (**B**)–(**K**) are presented as means with SEs ($n = 3$ independent experiments). *$P < 0.05$; **$P < 0.01$; ***$P < 0.001$

increased H3K18la modification in the PPARγ promoter region, whereas 2-DG blocked this effect (Fig. 5J, K). These findings indicate that hypoxia enhances glycolysis and lactate production in BM-MSCs, leading to elevated H3K18la levels in the PPARγ promoter region, activation of PPARγ gene transcription, and promotion of BM-MSC adipogenic differentiation.

The PPARγ inhibitor T0070907 can rescue CIH-induced long bone growth impairment

To investigate whether CIH-induced long bone growth inhibition results from increased PPARγ expression due to H3K18la upregulation, we applied the PPARγ inhibitor T0070907. The results showed that T0070907 reversed the CIH-induced increase in the BM-MSC adipogenic capacity and restored impaired osteogenic differentiation (Fig. 6A, B). qPCR analysis demonstrated that T0070907 rebalanced the disrupted adipogenic and osteogenic differentiation of BM-MSCs caused by CIH (Fig. 6C). Similarly, T0070907 improved the osteogenic capacity of BM-MSCs under hypoxic conditions (Fig. 6D-F).

Furthermore, we explored the effects of T0070907 in vivo. Our results revealed that, compared with the control group, the mice in the T0070907-treated group presented greater body weights and greater body and femur lengths (Fig. 6G-J). Compared with those of control mice, micro-CT images revealed that the trabecular bone region beneath the distal femoral growth plate presented an increased trabecular number, a more regular and denser arrangement, and increased trabecular interconnections following T0070907 treatment (Fig. 6K). Additionally, the BV/TV, Tb.N, and Tb.Th significantly increased in the T0070907-treated group, whereas the Tb.Sp and SMI somewhat decreased (Fig. 6L). Histological analysis showed that the length of the PZ of the femoral growth plate was increased in T0070907-treated mice, with a greater number of proliferating cells, whereas the HZ and RZ remained unchanged (Fig. 6M, N). Moreover, ELISA analysis revealed that the levels of serum bone formation markers were significantly greater in the T0070907-treated group than in the control group, whereas the levels of bone resorption markers increased only slightly following T0070907 treatment (Fig. 6O). These findings indicate that T0070907 can rescue CIH-induced long bone growth impairment.

Discussion

Pediatric obstructive sleep apnea–hypopnea syndrome is a common condition affecting children's health, and the chronic intermittent hypoxia it induces significantly impacts growth, development, and overall health in adolescents [6, 19]. Although the detrimental effects of OSAS on bone development and metabolism have been recognized, the underlying mechanisms still require further exploration. In this study, we found that CIH significantly impaired the osteogenic differentiation of BM-MSCs and long bone growth. Mechanistically, CIH increases H3K18la levels in the PPARγ promoter region, leading to increased PPARγ expression, which disrupts the balance of BM-MSC differentiation and inhibits BM-MSC osteogenesis. Our investigation reveals, at least in part, the molecular basis of CIH-induced long bone developmental impairment.

The effects of CIH on bone growth and metabolism remain unclear. Some studies suggest that OSAS may impair bone density [19, 20], whereas others report no evidence of a relationship between OSAS and bone metabolic damage [21]. These conflicting clinical findings may be attributed to biases such as age, sex, weight, and health status, as well as potential confounding variables. To reduce the impact of these confounding factors in clinical patients, the present study established a mouse model of CIH to investigate its effects on long bone development. Our results showed that CIH exposure during the critical long bone growth period (4–8 weeks of age) significantly inhibited bone growth, as evidenced by shorter body and femur lengths, and decreased trabecular bone density in the distal femurs of CIH-treated mice. Previous studies have indicated that hypoxia can disrupt endochondral ossification, a process essential for longitudinal bone growth, by inhibiting chondrocyte proliferation [22, 23]. Consistently, our histological analysis revealed a significant reduction in the proliferative zone of the

femoral growth plate in CIH-treated mice, along with a decrease in the number of proliferative chondrocytes. In addition, our study demonstrated that CIH reduces the expression levels of both serum osteogenic and osteoclastic markers, with a more significant reduction in the expression of osteogenic markers. These findings suggest that CIH primarily inhibits long bone growth by impairing the osteogenic process.

Next, we investigated how CIH affects long bone growth. Research has shown that hypoxia-induced HIF-1α activation shifts the bone microenvironment toward excessive angiogenesis, thereby impairing osteogenesis [24]. Dou et al. reported that CIH triggers metabolic bone disorders by activating the bone cannabinoid receptor 1 (CB1R) [25]. Our single-cell transcriptomic analysis revealed a significant reduction in the proportion of osteoprogenitors in CIH-treated mice, with adipogenic differentiation-related pathways enriched in BM-MSCs. Similarly, our metabolomic analysis of femoral tissue confirmed the upregulation of adipogenic differentiation pathways and the suppression of osteogenic differentiation pathways. Numerous studies have indicated that disruption of BM-MSC differentiation homeostasis contributes to various common skeletal diseases. Research has shown that imbalanced BM-MSC differentiation leads to age-related bone loss accompanied by an increase in bone marrow fat [26]. The antileprosy drug clofazimine has been found to cause osteopenia in long bones, characterized by suppressed osteoblast function due to enhanced adipogenesis [27]. Conversely, BM-MSCs from patients with malignant infantile osteopetrosis (MIOP) exhibit a defect in differentiation toward the adipogenic lineage, leading to impaired bone remodeling and abnormally increased bone density [28].

Histone lactylation is a recently discovered post-translational modification that was first reported in 2019 [29]. Abnormal histone lactylation is a key hallmark of numerous diseases, such as cancer and inflammatory disorders, and provides new insights into targeted therapies for these conditions [30]. Histone lactylation is dependent on lactate levels. Glycolysis inhibitors can reduce histone lactylation by decreasing lactate production, whereas hypoxia or aerobic respiration inhibitors can enhance histone lactylation by increasing lactate generation [31]. Our study revealed that the CIH mouse model induces a hypoxic state in femoral tissue, leading to increased glycolysis and elevated lactate concentrations. Furthermore we revealed that CIH-induced lactate accumulation increases H3K18la levels in the promoter region of the key adipogenic gene PPARγ, thereby activating PPARγ transcription and disrupting BM-MSC differentiation homeostasis. Notably, H3K18la induced by CIH may regulate multiple genes across the genome. In future studies, we aim to employ a ChIP-seq assay to identify genome-wide targets of H3K18la, providing new insights into the mechanisms underlying CIH-induced long bone growth impairment. In addition, current research suggests a complex interplay between histone lactylation and histone acetylation [32]. The histone acetyltransferase P300 mediates histone lactylation, whereas the enzymes responsible for histone delactylation belong to the HDAC (histone deacetylase) family [29]. Studies have shown that lactylation and acetylation at the same histone site may compete with each other [33]. Whether this competition plays a regulatory role in CIH-induced long bone growth inhibition remains to be investigated in future research. Finally, our results indicate that the PPARγ inhibitor, T0070907, can partially rescue long bone dysplasia induced by CIH in mice, demonstrating promising translational potential. However, PPARγ plays a wide-ranging role in various biological processes. As a ligand-activated nuclear receptor, PPARγ primarily functions to regulate lipid metabolism, adipogenesis, and glucose homeostasis [34]. For example, PPARγ is considered a crucial metabolic regulator of hepatic lipid metabolism and inflammation [35]. In addition, PPARγ can initiate adipose tissue browning and thermogenesis through its interaction with the coactivator PR domain-containing protein 16 (PRDM16) [36]. In addition to its metabolic functions, PPARγ also modulates immune responses and has been implicated in various pathological conditions, including allergic diseases [37] and certain cancers [38]. Therefore, PPARγ inhibitors may influence these biological processes, which warrants further investigation. In our future studies, a comprehensive evaluation of the safety of PPARγ-targeted therapy will be highly important, particularly regarding its impacts on major organ functions, systemic glucose and lipid metabolism, inflammatory responses, and pharmacokinetics.

Conclusions

In conclusion, our results revealed that CIH impaired long bone growth in growing mice. Further analyses indicated that CIH enhances glycolysis and lactate production in BM-MSCs, consequently increasing the H3K18la level in the promoter region of PPARγ, leading to its transcriptional activation. As a result, the balance of BM-MSC differentiation is disrupted, thereby inhibiting osteogenic differentiation. Additionally, we confirmed that the PPARγ inhibitor T0070907 can mitigate CIH-induced long bone growth impairment. Our findings provide targeted therapeutic strategies to counteract hypoxia-induced skeletal impairments.

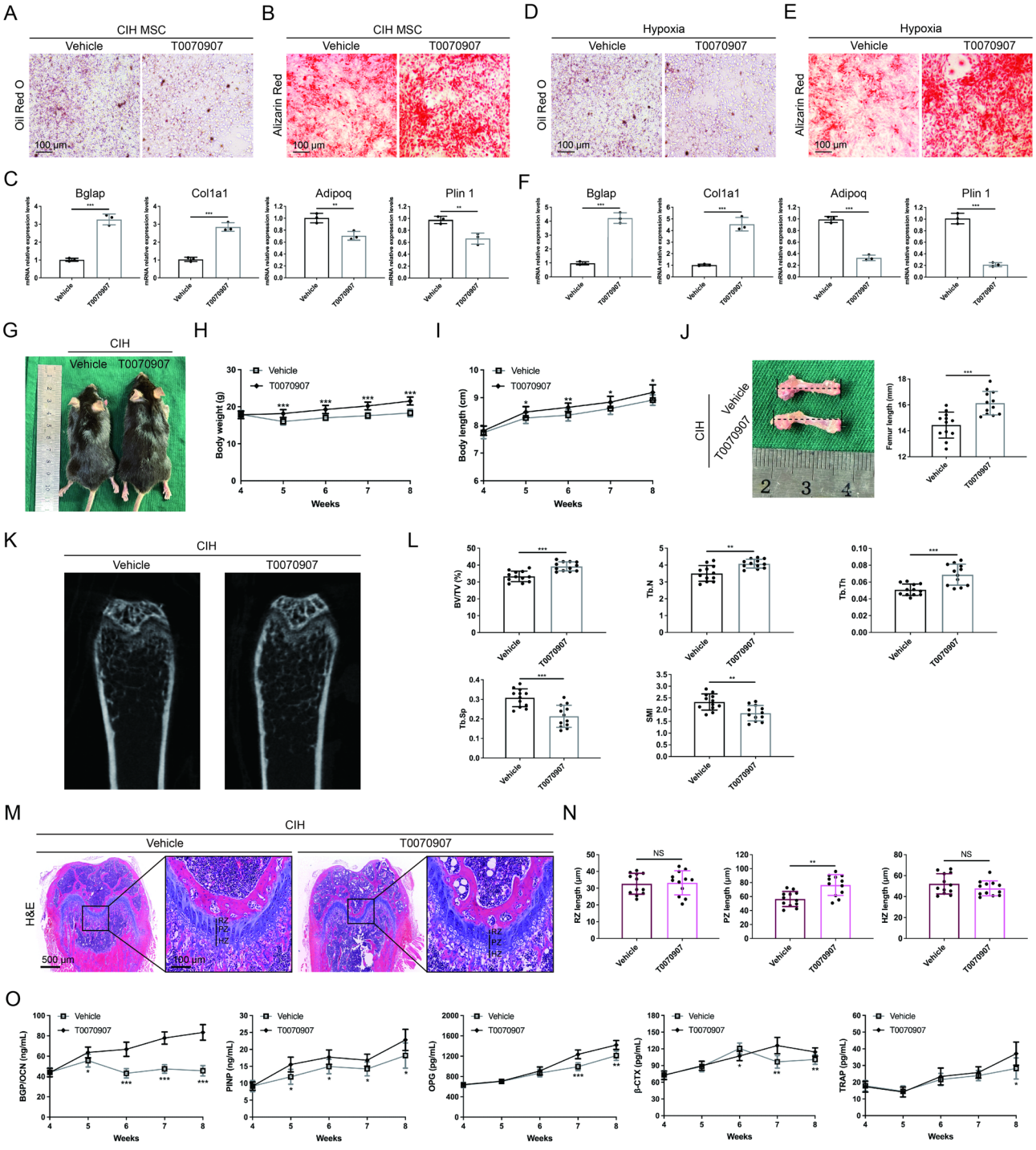

Fig. 6 Application of the PPARγ inhibitor T0070907 alleviates CIH-induced long bone growth impairment. (**A**, **B**) Oil Red O and Alizarin Red staining images of BM-MSCs isolated from CIH-treated mice with or without T0070907 treatment. (scale bar = 100 μm). (**C**) Relative RNA expression levels of osteogenic and adipogenic marker genes in BM-MSCs isolated from CIH-treated mice with or without T0070907 treatment. (**D**, **E**) Oil Red O and Alizarin Red staining images of BM-MSCs under hypoxic conditions with or without T0070907 treatment. (scale bar = 100 μm). (**F**) Relative RNA expression levels of osteogenic and adipogenic marker genes in BM-MSCs under hypoxic conditions with or without T0070907 treatment. (**G**) Macroscopic images of CIH-treated mice with or without T0070907 treatment. (**H**, **I**) The quantification of body weight and body length at all examined time points. (**J**) Macroscopic images of the mouse femur and quantification of femur length. (**K**) Micro-CT images of the femur from CIH-treated mice with or without T0070907 treatment. (**L**) The quantification of BV/TV%, Tb.N, Tb.Th, Tb.Sp and SMI. (**M**) H&E-stained images of the distal femur from CIH-treated mice with or without T0070907 treatment. (scale bar = 500 μm). Zoomed-in images show the growth plate cartilage region. (zoom scale bar = 100 μm). (**N**) The quantification of the lengths of RZ, PZ, and HZ. (**O**) Serum bone turnover marker levels at all examined time points. Data in (**C**) and (**F**) are presented as means with SEs ($n = 3$ independent experiments). Data in (**G**)–(**O**) are presented as mean ± SD ($n = 12$ biologically independent animals). $^{*}P < 0.05$; $^{**}P < 0.01$; $^{***}P < 0.001$

Abbreviations

OSAS	Obstructive Sleep Apnea Syndrome
CIH	Chronic intermittent hypoxia
BM-MSCs	Bone marrow mesenchymal stem cells
BMP	Bone morphogenetic protein
BV/TV%	Bone volume per tissue volume
Tb.N	Trabecular number
Tb.Th	Trabecular thickness
Tb.Sp	Trabecular separation
SMI	Structure model index
PZ	Proliferative zone
HZ	Hypertrophic zone
RZ	Resting zone
OCN	Osteocalcin
OSX	Osterix
PINP	Procollagen I N-terminal propeptide
β-CTX	β-cross-linked ctelopeptide of type I collagen
TRAP	Tartrate-resistant acid phosphatase
OPG	Osteoprotegerin

Acknowledgements
None.

Author contributions
Conceptualization: F.C., M.Z.G., S.S.Z., and X.Y.L. Data curation: F.C., M.Z.G., H.M.X., and X.Y.L. Formal analysis: F.C., M.Z.G., S.S.Z., X.Y.L and L.C.D. Funding acquisition: F.C., H.M.X., and P.L. Investigation: F.C., M.Z.G., and Z.L.S. Methodology: F.C., M.Z.G., H.M.X., and S.S.Z. Resources: F.C., and S.S.Z. Software: F.C., S.S.Z., and Z.L.S. Supervision: X.Y.L, L.C.D., and P.L. Validation: F.C., Z.L.S., X.Y.L, L.C.D., and P.L. Visualization: F.C., X.Y.L, L.C.D., and P.L. Writing– original draft: F.C., M.Z.G., X.Y.L, L.C.D., and P.L. Writing– review & editing: F.C., M.Z.G., H.M.X., S.S.Z., Z.L.S., X.Y.L, L.C.D., P.L. All authors approved the final manuscript.

Funding
This study was supported by the General Program of the National Natural Science Foundation of China (No. 81871131) (P.L.), (No.82171121) (H.M.X.); the China International Medical Foundation (z-2019-41-2201) (F.C.)

Data availability
The data that support the findings of this study are available within the article or from the corresponding author upon reasonable request.

Declarations

Ethics approval and consent to participate
The study was approved by the Ethics Committee of Shanghai Sixth People's Hospital (No. 2024 – 0632).

Consent for publication
Not applicable.

Competing interests
The authors confirm that there are no conflicts of interest.

Received: 20 April 2025 / Accepted: 9 July 2025
Published online: 28 July 2025

References

1. Benjafield AV, Ayas NT, Eastwood PR, Heinzer R, Ip MSM, Morrell MJ, et al. Estimation of the global prevalence and burden of obstructive sleep apnoea: a literature-based analysis. Lancet Respir Med. 2019;7(8):687–98. https://doi.org/10.1016/S2213-2600(19)30198-5
2. Bitners AC, Arens R. Evaluation and management of children with obstructive sleep apnea syndrome. Lung. 2020;198(2):257–70. https://doi.org/10.1007/s00408-020-00342-5
3. Zhang K, Ma D, Wu Y, Xu Z. Impact of chronic intermittent hypoxia on cognitive function and hippocampal neurons in mice: A study of inflammatory and oxidative stress pathways. Nat Sci Sleep. 2024;16:2029–43. https://doi.org/10.2147/NSS.S489232
4. Wang F, Zou J, Xu H, Huang W, Zhang X, Wei Z, et al. Effects of chronic intermittent hypoxia and chronic sleep fragmentation on gut microbiome, serum metabolome, liver and adipose tissue morphology. Front Endocrinol (Lausanne). 2022;13:820939. https://doi.org/10.3389/fendo.2022.820939
5. Vanek J, Prasko J, Genzor S, Ociskova M, Kantor K, Holubova M, et al. Obstructive sleep apnea, depression and cognitive impairment. Sleep Med. 2020;72:50–8. https://doi.org/10.1016/j.sleep.2020.03.017
6. Serebrovskaya TV, Xi L. Intermittent hypoxia in childhood: the harmful consequences versus potential benefits of therapeutic uses. Front Pediatr. 2015;3:44. https://doi.org/10.3389/fped.2015.00044
7. Sivaraj KK, Jeong HW, Dharmalingam B, Zeuschner D, Adams S, Potente M, et al. Regional specialization and fate specification of bone stromal cells in skeletal development. Cell Rep. 2021;36(2):109352. https://doi.org/10.1016/j.celrep.2021.109352
8. Ning K, Liu S, Yang B, Wang R, Man G, Wang DE, et al. Update on the effects of energy metabolism in bone marrow mesenchymal stem cells differentiation. Mol Metab. 2022;58:101450. https://doi.org/10.1016/j.molmet.2022.101450
9. Yellowley CE, Genetos DC. Hypoxia signaling in the skeleton: implications for bone health. Curr Osteoporos Rep. 2019;17(1):26–35. https://doi.org/10.1007/s11914-019-00500-6
10. Li Y, Hu M, Xie J, Li S, Dai L. Dysregulation of histone modifications in bone marrow mesenchymal stem cells during skeletal ageing: roles and therapeutic prospects. Stem Cell Res Ther. 2023;14(1):166. https://doi.org/10.1186/s13287-023-03393-6
11. Wang Y, Deng P, Liu Y, Wu Y, Chen Y, Guo Y, et al. Alpha-ketoglutarate ameliorates age-related osteoporosis via regulating histone methylations. Nat Commun. 2020;11(1):5596. https://doi.org/10.1038/s41467-020-19360-1
12. Wang J, Wang CD, Zhang N, Tong WX, Zhang YF, Shan SZ, et al. Mechanical stimulation orchestrates the osteogenic differentiation of human bone marrow stromal cells by regulating HDAC1. Cell Death Dis. 2016;7(5):e2221. https://doi.org/10.1038/cddis.2016.112
13. Zhang C, Zhou L, Zhang M, Du Y, Li C, Ren H, et al. H3K18 lactylation potentiates immune escape of Non-Small cell lung Cancer. Cancer Res. 2024;84(21):3589–601. https://doi.org/10.1158/0008-5472.CAN-23-3513
14. Rho H, Terry AR, Chronis C, Hay N. Hexokinase 2-mediated gene expression via histone lactylation is required for hepatic stellate cell activation and liver fibrosis. Cell Metab. 2023;35(8):1406–e238. https://doi.org/10.1016/j.cmet.2023.06.013
15. Pan RY, He L, Zhang J, Liu X, Liao Y, Gao J, et al. Positive feedback regulation of microglial glucose metabolism by histone H4 lysine 12 lactylation in alzheimer's disease. Cell Metab. 2022;34(4):634–e486. https://doi.org/10.1016/j.cmet.2022.02.013
16. Li X, Wang F, Gao Z, Huang W, Zhang X, Liu F, et al. Melatonin attenuates chronic intermittent hypoxia-induced intestinal barrier dysfunction in mice. Microbiol Res. 2023;276:127480. https://doi.org/10.1016/j.micres.2023.127480
17. Sun J, Du J, Feng W, Lu B, Liu H, Guo J, et al. Histological evidence that Metformin reverses the adverse effects of diabetes on orthodontic tooth movement in rats. J Mol Histol. 2017;48(2):73–81. https://doi.org/10.1007/s10735-016-9707-y
18. Zhang H, Huang J, Liu J, Li Y, Gao Y. BMMSC-sEV-derived miR-328a-3p promotes ECM remodeling of damaged urethral sphincters via the Sirt7/TGFbeta signaling pathway. Stem Cell Res Ther. 2020;11(1):286. https://doi.org/10.1186/s13287-020-01808-2
19. Uzkeser H, Yildirim K, Aktan B, Karatay S, Kaynar H, Araz O, et al. Bone mineral density in patients with obstructive sleep apnea syndrome. Sleep Breath. 2013;17(1):339–42. https://doi.org/10.1007/s11325-012-0698-y
20. Tomiyama H, Okazaki R, Inoue D, Ochiai H, Shiina K, Takata Y, et al. Link between obstructive sleep apnea and increased bone resorption in men. Osteoporos Int. 2008;19(8):1185–92. https://doi.org/10.1007/s00198-007-0556-0
21. Mariani S, Fiore D, Varone L, Basciani S, Persichetti A, Watanabe M, et al. Obstructive sleep apnea and bone mineral density in obese patients. Diabetes Metab Syndr Obes. 2012;5:395–401. https://doi.org/10.2147/DMSO.S37761
22. Leijten JC, Moreira Teixeira LS, Landman EB, van Blitterswijk CA, Karperien M. Hypoxia inhibits hypertrophic differentiation and endochondral ossification in explanted tibiae. PLoS ONE. 2012;7(11):e49896. https://doi.org/10.1371/journal.pone.0049896
23. Lee HH, Chang CC, Shieh MJ, Wang JP, Chen YT, Young TH, et al. Hypoxia enhances chondrogenesis and prevents terminal differentiation through PI3K/Akt/FoxO dependent anti-apoptotic effect. Sci Rep. 2013;3:2683. https://doi.org/10.1038/srep02683

24. Dirckx N, Tower RJ, Mercken EM, Vangoitsenhoven R, Moreau-Triby C, Breugelmans T, et al. Vhl deletion in osteoblasts boosts cellular Glycolysis and improves global glucose metabolism. J Clin Invest. 2018;128(3):1087–105. https://doi.org/10.1172/JCI97794
25. Dou ZJ, Gao XL, Jia YL, Chen J, Yang JJ, Chen Y, et al. CB1 receptor antagonist Rimonabant protects against chronic intermittent hypoxia-induced bone metabolism disorder and destruction in rats. Sleep Breath. 2020;24(4):1441–9. https://doi.org/10.1007/s11325-019-02009-9
26. Tian L, Lu L, Meng Y. Bone marrow stromal stem cell fate decision: A potential mechanism for bone marrow adipose increase with Aging-related osteoporosis. Curr Mol Med. 2023;23(10):1046–57. https://doi.org/10.2174/1566524023666221025104629
27. Porwal K, Pal S, Tewari D, Pal China S, Singh P, Chandra Tewari M, et al. Increased bone Marrow-Specific adipogenesis by Clofazimine causes impaired fracture healing, osteopenia, and osteonecrosis without extraskeletal effects in rats. Toxicol Sci. 2019;172(1):167–80. https://doi.org/10.1093/toxsci/kfz172
28. Uckan D, Kilic E, Sharafi P, Kazik M, Kaya F, Erdemli E, et al. Adipocyte differentiation defect in mesenchymal stromal cells of patients with malignant infantile osteopetrosis. Cytotherapy. 2009;11(4):392–402. https://doi.org/10.1080/14653240802582083
29. Zhang D, Tang Z, Huang H, Zhou G, Cui C, Weng Y, et al. Metabolic regulation of gene expression by histone lactylation. Nature. 2019;574(7779):575–80. https://doi.org/10.1038/s41586-019-1678-1
30. Sun L, Zhang Y, Yang B, Sun S, Zhang P, Luo Z, et al. Lactylation of METTL16 promotes Cuproptosis via m(6)A-modification on FDX1 mRNA in gastric cancer. Nat Commun. 2023;14(1):6523. https://doi.org/10.1038/s41467-023-42025-8
31. Izzo LT, Wellen KE. Histone lactylation links metabolism and gene regulation. Nature. 2019;574(7779):492–3. https://doi.org/10.1038/d41586-019-03122-1
32. Zhu J, Wu X, Mu M, Zhang Q, Zhao X. TEC-mediated tRF-31R9J regulates histone lactylation and acetylation by HDAC1 to suppress hepatocyte ferroptosis and improve non-alcoholic steatohepatitis. Clin Epigenetics. 2025;17(1):9. https://doi.org/10.1186/s13148-025-01813-3
33. Dai X, Lv X, Thompson EW, Ostrikov KK. Histone lactylation: epigenetic mark of glycolytic switch. Trends Genet. 2022;38(2):124–7. https://doi.org/10.1016/j.tig.2021.09.009
34. Szanto M, Gupte R, Kraus WL, Pacher P, Bai P. PARPs in lipid metabolism and related diseases. Prog Lipid Res. 2021;84:101117. https://doi.org/10.1016/j.plipres.2021.101117
35. Chen H, Tan H, Wan J, Zeng Y, Wang J, Wang H, et al. PPAR-gamma signaling in nonalcoholic fatty liver disease: pathogenesis and therapeutic targets. Pharmacol Ther. 2023;245:108391. https://doi.org/10.1016/j.pharmthera.2023.108391
36. Zhong Y, Wang Y, Li X, Qin H, Yan S, Rao C, et al. PRMT4 facilitates white adipose tissue Browning and thermogenesis by methylating PPARgamma. Diabetes. 2023;72(8):1095–111. https://doi.org/10.2337/db22-1016
37. Stark JM, Coquet JM, Tibbitt CA. The role of PPAR-gamma in allergic disease. Curr Allergy Asthma Rep. 2021;21(11):45. https://doi.org/10.1007/s11882-021-01022-x
38. Hartley A, Ahmad I. The role of PPARgamma in prostate cancer development and progression. Br J Cancer. 2023;128(6):940–5. https://doi.org/10.1038/s41416-022-02096-8

Publisher's note